STM JOURNALS

Journal of
Polymer & Composites

ISSN: 2321-2810 (Online)
ISSN: 2321-8525 (Print)
Volume 14, Issue 4, 2026
DOI (Journal): 10.37591/JoPC

https://journals.stmjournals.com/jopc

Research JoPC

Dissipative Particle Dynamics Simulation Study on the Evolution of Photoinitiated Free Radical Polymerization Crosslinked Networks

Bingbing Pan[1], Zihua Liu[2], Yiyi Zhang[3], Wen Li[4], Hui Li[5]*

Abstract

Gradient polymer materials overcome the limitations of conventional homogeneous polymers by integrating multiple distinct functionalities within a single continuous structure. Although photoinitiated free-radical polymerization offers excellent spatial and temporal control, the underlying microscopic mechanisms governing network evolution under non-uniform light fields remain poorly understood. In this study, a mesoscale dissipative particle dynamics (DPD) model was successfully developed to couple free-radical polymerization kinetics—including initiation, propagation, crosslinking, and termination—with exponential light attenuation along the z-axis via the Lambert–Beer law, characterized by a dimensionless parameter k. The simulation results systematically demonstrate that light attenuation acts as the fundamental driver of gradient structure formation by restricting local radical generation. Increasing k confines radical initiation primarily to the near-light region, thereby inducing a pronounced spatial asynchrony in monomer consumption and chain propagation. This severe kinetic heterogeneity yields a distinct topological gradient under strong attenuation: the near-light region forms a dense network characterized by short-chain, highly crosslinked domains, whereas the far-light region features longer chains and a loose morphology. Notably, strong light attenuation creates an environment where localized growing chains compete intensely for crosslinkers, significantly enhancing crosslinking site utilization efficiency. These molecular-level insights provide crucial theoretical guidance and a predictive framework for the rational design and controllable fabrication of advanced gradient polymer materials.

***Author for Correspondence**
Hui Li
E-mail: lihuidhg@lut.edu.cn

[1]Graduate Student, School of Material Science and Engineering, LanZhou University of Technology, LanZhou, China
[2]Undergraduate Student, School of Material Science and Engineering, LanZhou University of Technology, LanZhou, China
[3]Graduate Student, School of Material Science and Engineering, LanZhou University of Technology, LanZhou, China
[4]Graduate Student, School of Material Science and Engineering, LanZhou University of Technology, LanZhou, China
[5]Professor, School of Material Science and Engineering, LanZhou University of Technology, LanZhou, China

Received Date: June 18, 2026
Accepted Date: June 22, 2026
Published Date: July 02, 2026

Citation: Bingbing Pan, Zihua Liu, Yiyi Zhang, Wen Li, Hui Li. Dissipative Particle Dynamics Simulation Study on the Evolution of Photoinitiated Free Radical Polymerization Crosslinked Networks. Journal of Polymer & Composites. 2026; 14(4): 142–158p.

Keywords: Gradient polymer materials; photoinitiated radical polymerization; crosslinked network structure; competitive mechanism; mesoscale simulation

INTRODUCTION

Gradient polymer materials possess continuously varying structures or compositions along a spatial direction, enabling the integration of multiple functionalities within a single material. Such structural heterogeneity allows different regions of the material to exhibit distinct properties simultaneously, thereby overcoming the limitations of conventional homogeneous polymers in property design and functional integration [1]. In recent years, gradient polymer materials have attracted considerable attention owing to their promising applications in biomedical materials, [2–14] coating systems, [15–18] and flexible electronic devices [19–30].

Various strategies have been developed to fabricate gradient polymer structures, including layer-by-layer assembly, diffusion-controlled processing, self-assembly-induced methods, and external-field regulation [31]. Among these approaches, photoinitiated free-radical polymerization has emerged as one of the most widely employed techniques because of its excellent spatial and temporal controllability [32–34]. For example, Tu et al. [35] fabricated gradient-index (GRIN) polymer optical materials using grayscale digital light processing (DLP) photopolymerization. By controlling the light dosage in different regions, spatial variations in monomer conversion were generated, resulting in a refractive-index gradient. Wen et al. [36] developed an anthracene-containing photosensitive liquid crystal elastomer (AnLCE), in which ultraviolet light attenuation within the material induced a higher degree of photocrosslinking near the irradiated surface. Consequently, a gradient network structure characterized by a stiff, highly crosslinked surface layer and a less crosslinked interior region was formed. Despite the successful fabrication of various gradient polymer materials through light-field regulation, the microscopic mechanisms governing gradient formation remain insufficiently understood. In particular, multiple kinetic processes, including radical generation, chain propagation, chain termination, and crosslinking reactions, occur simultaneously and compete throughout the polymerization process. The coupling among these reactions ultimately determines the evolution of network structures and the resulting material properties. However, due to the limitations of experimental characterization techniques, the spatiotemporal distribution of radicals, the utilization efficiency of crosslinking sites, and the evolution of network topology are difficult to observe directly. Therefore, elucidating the intrinsic relationship between heterogeneous reaction kinetics and network structure formation under non-uniform light fields at the mesoscale is of considerable importance for the controllable fabrication of gradient polymer materials.

Computational simulation techniques, particularly mesoscale coarse-grained approaches, [37–40] provide an effective means to investigate these issues. By sacrificing a portion of atomistic detail, these methods substantially extend the accessible temporal and spatial scales, enabling the capture of the statistical characteristics of polymerization reactions and structural evolution. Dissipative particle dynamics (DPD) is a representative mesoscale simulation method that explicitly incorporates fluctuation–dissipation effects and accurately reproduces hydrodynamic behavior [41]. It has been extensively applied to studies of polymer self-assembly and polymerization processes. Nevertheless, most existing simulation studies on radical polymerization have focused on homogeneous reaction environments [42, 43]. Systematic investigations into polymerization kinetics, network structure evolution, and their relationship with material properties under non-uniform light fields, which constitute a key source of gradient formation, remain scarce.

Motivated by these considerations, a mesoscale DPD model explicitly coupling non-uniform light attenuation with free-radical polymerization kinetics was developed in this work. The Lambert–Beer law was introduced to describe the exponential decay of light intensity along the propagation direction, and a dimensionless parameter, k, was employed to characterize the attenuation strength. The influences of light-field conditions on radical generation, monomer consumption, and the evolution of crosslinked network topology were systematically investigated. The results provide valuable simulation insights for the rational design and fabrication of gradient polymer materials.

SIMULATION METHODS AND MODEL

Dissipative Particle Dynamics

To describe the spatially non-uniform evolution of cross-linked networks during light-field-induced gradient radical polymerization, this paper employs the dissipative particle dynamics (DPD) method [44] to construct a mesoscale simulation model. This method preserves mass and momentum conservation while explicitly incorporating thermal noise and dissipation, enabling the description of mesoscopic-scale temporal and spatial dynamics in soft matter systems. It finds extensive application in studies of polymer solutions, self-assembled systems, and interfacial and phase separation behaviors [41, 45, 46]. Although the coarse-grained model omits certain atomic-level details, it effectively

describes the system's kinetic evolution and statistical characteristics of the cross-linked network structure at the mesoscopic scale. This makes it well-suited for investigating the evolution of gradient cross-linked network structures induced by light fields. In DPD, the motion of all particles follows Newton's equations of motion:

$$\frac{d\,\mathrm{r}_i}{d\,t} = \mathrm{v}_i,\ \frac{d\,\mathrm{v}_i}{d\,t} = \mathrm{f}_i \tag{1}$$

where r_i、v_i, and f_i denote respectively the position, velocity, and force acting upon particle i of mass m at time t. In DPD, the expression for the force acting upon a bead is given by:

$$\mathrm{f}_i = \sum_{i \neq j}(\mathrm{F}_{ij}^{\mathrm{C}}+\mathrm{F}_{ij}^{\mathrm{D}}+\mathrm{F}_{ij}^{\mathrm{R}}) \tag{2}$$

where $\mathrm{F}_{ij}^{\mathrm{C}}$ denotes the conservative force, $\mathrm{F}_{ij}^{\mathrm{D}}$ denotes the dissipative force, and $\mathrm{F}_{ij}^{\mathrm{R}}$ denotes the random force. Their expressions are:

$$\mathrm{F}_{ij}^{\mathrm{C}} = a_{ij}w^{\mathrm{C}}(r_{ij})\hat{\mathrm{r}}_{ij} \tag{3}$$

$$\mathrm{F}_{ij}^{\mathrm{D}} = -\gamma w^{\mathrm{D}}(r_{ij})(\mathrm{v}_{ij}\cdot\hat{\mathrm{r}}_{ij})\hat{\mathrm{r}}_{ij} \tag{4}$$

$$\mathrm{F}_{ij}^{\mathrm{R}} = \sigma' w^{\mathrm{R}}(r_{ij})\zeta_{ij}\Delta t^{-1/2}\hat{\mathrm{r}}_{ij} \tag{5}$$

where a_{ij} is the repulsive coefficient between particles, r_{ij} is the distance between particles, $\hat{\mathrm{r}}_{ij}$ is the unit vector direction, γ is the dissipation coefficient, v_{ij} is the relative velocity, σ' is the noise intensity, and ζ_{ij} is a random variable with zero mean and unit variance. In the equation, $w^{\mathrm{C}}(r_{ij})$, $w^{D}(r_{ij})$ and $w^{\mathrm{R}}(r_{ij})$ represent the weighting functions for conservative forces, dissipative forces, and random forces, respectively. When $r_c < r_{ij}$, $w^{\mathrm{C}}(r_{ij}) = (1 - r_{ij}/r_c)$, otherwise it is 0; Maintaining the system's thermodynamic stability via the Fluctuation–Dissipation Theorem [47]:

$$\sigma'^2 = 2\gamma k_B T,\ w^{\mathrm{D}}(r_{ij}) = [w^{\mathrm{R}}(r_{ij})]^2 \tag{6}$$

where k_B denotes the Boltzmann constant, while $w^{\mathrm{D}}(r_{ij})$ and $w^{\mathrm{R}}(r_{ij})$ adopt the classical form [48]:

$$w^{\mathrm{D}}(r_{ij}) = [w^{\mathrm{R}}(r_{ij})]^2 = \begin{cases} (1-\frac{r_{ij}}{r_c})^2, & r_{ij}<r_c \\ 0, & r_{ij}\geq r_c \end{cases} \tag{7}$$

Where r_c denotes the interaction cutoff radius. For numerical convenience, in this simulation $r_c = k_B T = m = 1.0$. The bond potential between beads employs the finite extensible non-linear elastic (FENE) potential function model [49]:

$$U_{FENE}(r) = -\frac{1}{2}k' R_0^2 ln\left[1-\left(\frac{r}{R_0}\right)^2\right],\ r < R_0 \tag{8}$$

where the stiffness coefficient k' is set to 30.0, and the maximum key length R_0 is set to 1.5σ, where σ denotes the simplified length unit。The Newtonian equations of motion are integrated using the Groot–Warren-Velocity Verlet algorithm (GW-VV) [41, 50]:

$$\mathrm{r}_i(t+\Delta t)=\mathrm{r}_i(t)+\Delta t\ \mathrm{v}_i(t)+\frac{1}{2}(\Delta t)^2\mathrm{f}_i(t) \tag{9}$$

$$\tilde{\mathrm{v}}_i(t+\Delta t)=\mathrm{v}_i(t)+\lambda\Delta t\ \mathrm{f}_i(t) \tag{10}$$

$$\mathrm{f}_i(t+\Delta t)=\mathrm{f}_i[\mathrm{r}(t+\Delta t), \tilde{\mathrm{v}}(t+\Delta t)] \tag{11}$$

$$\mathrm{v}_i(t+\Delta t)=\mathrm{v}_i(t)+\frac{1}{2}\Delta t(\mathrm{f}_i(t)+\mathrm{f}_i(t+\Delta t)) \tag{12}$$

where λ is set to 0.65, the time step $\Delta t = 0.04$, and the time unit t is defined as $\tau = \sqrt{mr_c^2/k_B\mathrm{T}} = 1$.

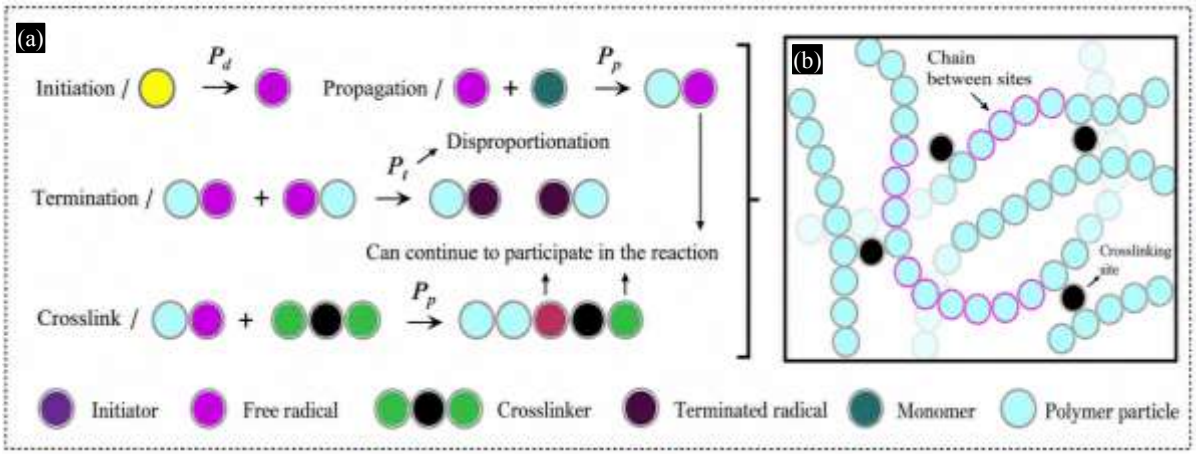

Figure 1. (a) Reaction model; (b) Schematic diagram of cross-linked network structure.

Free Radical Polymerization Reaction Models and Structural Characterization

In the present coarse-grained model, initiators, radicals, monomers, and solvent molecules are represented by individual DPD beads. Polymer chains are generated dynamically through the formation of chemical bonds between reactive particles during the simulation. The reaction scheme employed in this work is illustrated in Figure 1(a). Radical generation is initiated through the activation of initiator beads. At each simulation step, an initiator bead can transform into an active radical with a probability of P_d. Although practical photoinitiators generally undergo bond cleavage to produce two radical species upon irradiation, a simplified single-radical initiation mechanism was adopted here to improve computational efficiency and focus on the essential features of network formation [43, 51]. Once generated, the radical bead can react with nearby monomer beads. When the separation distance between a radical and a monomer satisfies $r \leq r_{cut} = 1.0\sigma$, a propagation event occurs with probability P_p. During this process, a new bond is formed, the activated monomer becomes the new chain-end radical, and the original radical site is converted into a non-reactive segment of the growing polymer chain. This mechanism allows radical activity to migrate continuously along the chain backbone during polymer growth. Chain termination is described by a disproportionation mechanism. When two active chain-end radicals approach within the reaction cutoff distance, termination may occur with probability P_t, resulting in the deactivation of both radical sites. Combination termination reactions were neglected in the present study. Once a bead becomes part of a terminated chain segment, it no longer participates in subsequent chemical reactions.

To construct a crosslinked network, a bifunctional crosslinker model was introduced. Each crosslinker consists of two reactive beads connected through a central inert bead. The reactive groups possess the same reactivity as monomer beads and can participate in propagation reactions under identical reaction criteria. Consequently, crosslinkers can connect different polymer chains and promote the formation of a three-dimensional network structure. The particle number density of the simulation box was fixed at 3, The monomer concentration was set to 0.2, which ensures the formation of a sufficiently developed network. Following the parameterization proposed by Furuya and Koga [42], the concentrations of initiator and crosslinker were defined as $c_{\text{initiator}} = 0.005 \times c_{\text{monomer}}$ and $c_{\text{crosslinker}} = 0.1 \times c_{\text{monomer}}$, respectively, while all remaining particles were treated as inert solvent beads. The propagation and termination probabilities were fixed at $P_p = 0.05$ and $P_t = 0.5$. The relative ratios among these three reaction probabilities were also adopted from Furuya and Koga [42], who emphasized that, compared with chain propagation, a sufficiently slow initiation process is essential for reproducing the characteristic kinetics of free-radical polymerization.

Figure 1(b) presents a schematic illustration of the crosslinked network structure. The molecular chain segment between two adjacent crosslinking sites (the black inert bead located at the center of each crosslinker) is highlighted with a pink frame. In this work, beyond analyzing the spatial distribution of

various particle types, we further determined the regional distribution of these molecular chains based on the coordinates of their centers of mass. Within each spatial region, the number of constituent beads in each chain segment—defined as the molecular chain length $L_{chain,}$ and its average value $\bar{L}$, was obtained to characterize the characteristic network size in different regions. Moreover, to quantitatively describe the uniformity of the network structure size distribution, a dispersity index $Đ$ of the inter-node chain length was introduced, which is defined as follows:

$$Đ = \frac{\sum(L_{chain}{}^2 \times n_{chain}) / \sum(L_{chain} \times n_{chain})}{\sum(L_{chain} \times n_{chain}) / \sum n_{chain}} \tag{13}$$

where L_{chain} denotes the molecular chain length between two adjacent sites, and n_{chain} represents the number of chains with a length of L_{chain}. This index characterizes the breadth of the network pore size distribution: a larger value indicates a higher degree of structural heterogeneity.

Light Decay Model Based on Lambert–Beer Law

In a Photoinitiated free radical polymerization system, the spatial distribution of the light field within the reaction medium is the key factor governing the heterogeneity of polymerization kinetics. For a medium containing a photoabsorbing species, the incident light is continuously absorbed during propagation, resulting in a gradual attenuation of light intensity with increasing penetration depth. This spatial decay behavior can be described by the Lambert–Beer law. Assuming that the light propagates unidirectionally along the z-axis, the local light intensity can be expressed as follows:

$$I(z) = I_0 \exp(-\varepsilon c z) \tag{15}$$

where ε is the molar absorption coefficient of the photoabsorber, c is its concentration, and z denotes the penetration depth along the direction of light propagation. In experimental systems, gradient polymerization with different gradient intensities is typically achieved by selecting photoabsorbers with different absorption coefficients or by adjusting their concentrations. In this work, a dimensionless parameter $k = \varepsilon c$ was introduced to uniformly characterize the degree of light attenuation. A one-dimensional illumination model along the z-axis was established, as illustrated in Figure 2. The simulation box size was set to 50×50×100. The incident light was assumed to enter from the top of the box and propagate along the negative z-direction. It should be emphasized that the reaction model employed herein serves as a phenomenological description of the photopolymerization process. By shifting the focus from specific atomistic chemical pathways to macroscopic light-attenuation probabilities, this treatment avoids the prohibitive computational cost of fully-atomistic simulations. The initiator activation probability P_d, defined in the aforementioned radical polymerization model, was coupled with the local light intensity I. At the top surface of the box, P_d was set to 5×10^{-5}, and it decayed along the z-axis according to the light attenuation relationship described in Equation (15). In this way, a position-dependent radical generation rate was introduced into the system.

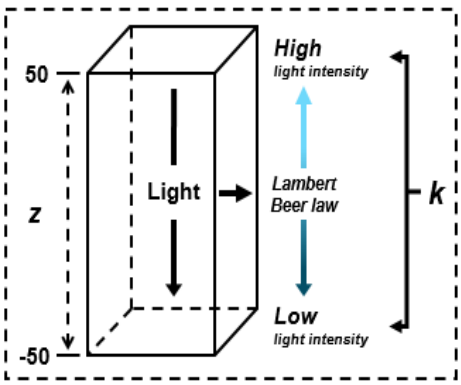

Figure 2. Light attenuation model based on Lambert–Beer law.

The attenuation strength of P_d throughout the system was controlled by adjusting the value of k. In this study, six values of k were systematically examined—0, 0.01, 0.02, 0.04, 0.08, and 0.16—to analyze the influence of the light-field gradient on free-radical polymerization kinetics and structural evolution. Each data point represents the average value of three independent simulations, with error bars indicating the corresponding standard deviation

Summary of Parameters

To ensure reproducible mesoscale modeling and clarity regarding the statistical mechanics of the coarse-grained environment, the fundamental operational criteria are consolidated below. Table 1 explicitly maps the system variables—categorized by spatial box configurations, chemical concentrations, localized reaction event stabilities, and dimensional light decay values—providing a cohesive parameter reference matrix for the coupled photopolymerization DPD environment.

RESULTS

Consumption of Monomers and Initiators Under Light Field Attenuation

Figure 3 presents the evolution of monomer conversion as a function of reaction time under different k conditions. To elucidate the spatial reaction heterogeneity induced by the exponential attenuation of light intensity along the z-direction, the simulation box was divided into two regions along the z-axis: the near-light region ("UP") and the far-light region ("Down"). The monomer consumption kinetics were statistically analyzed in each region separately. The results show that, with increasing k, enhanced light attenuation leads to an overall reduction in effective light intensity, thereby limiting the radical generation rate and significantly slowing the monomer consumption kinetics of the entire system. Under the no-attenuation condition ($k = 0$), the monomer conversion reaches 90% at approximately 0.5×10^5 simulation steps. In contrast, when k increases to 0.16, approximately 2.3×10^5 steps are required to reach the same conversion level (90%), indicating a pronounced decrease in reaction rate. A regional analysis further reveals that light attenuation exerts a more significant inhibitory effect on the "Down" region, thereby inducing a gradient in the polymer network. For example, when $k = 0.16$, the difference in monomer conversion between the "UP" and "Down" regions reaches a maximum at around 1×10^5 simulation steps. At this stage, the monomer conversion in the "UP" region is approximately 70%, entering a decelerated reaction regime, whereas that in the "Down" region is only about 50%. Even when the overall system conversion reaches 90%, the local conversions in the "UP" and "Down" regions are approximately 93% and 87%, respectively, maintaining a difference of about 6%. This indicates that the reaction gradient induced by light attenuation persists throughout the entire polymerization process.

Table 1. Summary of mesoscale coarse-grained simulation parameters, particle concentrations, and reaction mapping constants used in the DPD framework.

Parameter Category	Simulation parameter	Value / ratio	Description / source
System settings	Particle number density	3.0	Fixed system density
	Dimensionless temperature	1.0	Reduced energy unit
	Cutoff radius	1.0	Interaction range
	Time step	0.04	GW-VV integration step
Concentrations	Monomer concentration	0.2	Ensures network development
	Initiator concentration	$0.005\times c_{\text{monomer}}$	Particle density
	Crosslinker concentration	$0.1\times c_{\text{monomer}}$	
Reaction probabilities	Propagation probability (P_p)	0.05	Fixed rate for chain growth
	Termination probability (P_t)	0.5	Disproportionation mechanism
	Initiation probability (P_d)	5×10^{-5}	Defined at the top surface (z = 50)
Light field	Attenuation coefficient (k)	0, 0.01, 0.02, 0.04, 0.08, 0.16	Investigated gradient intensities

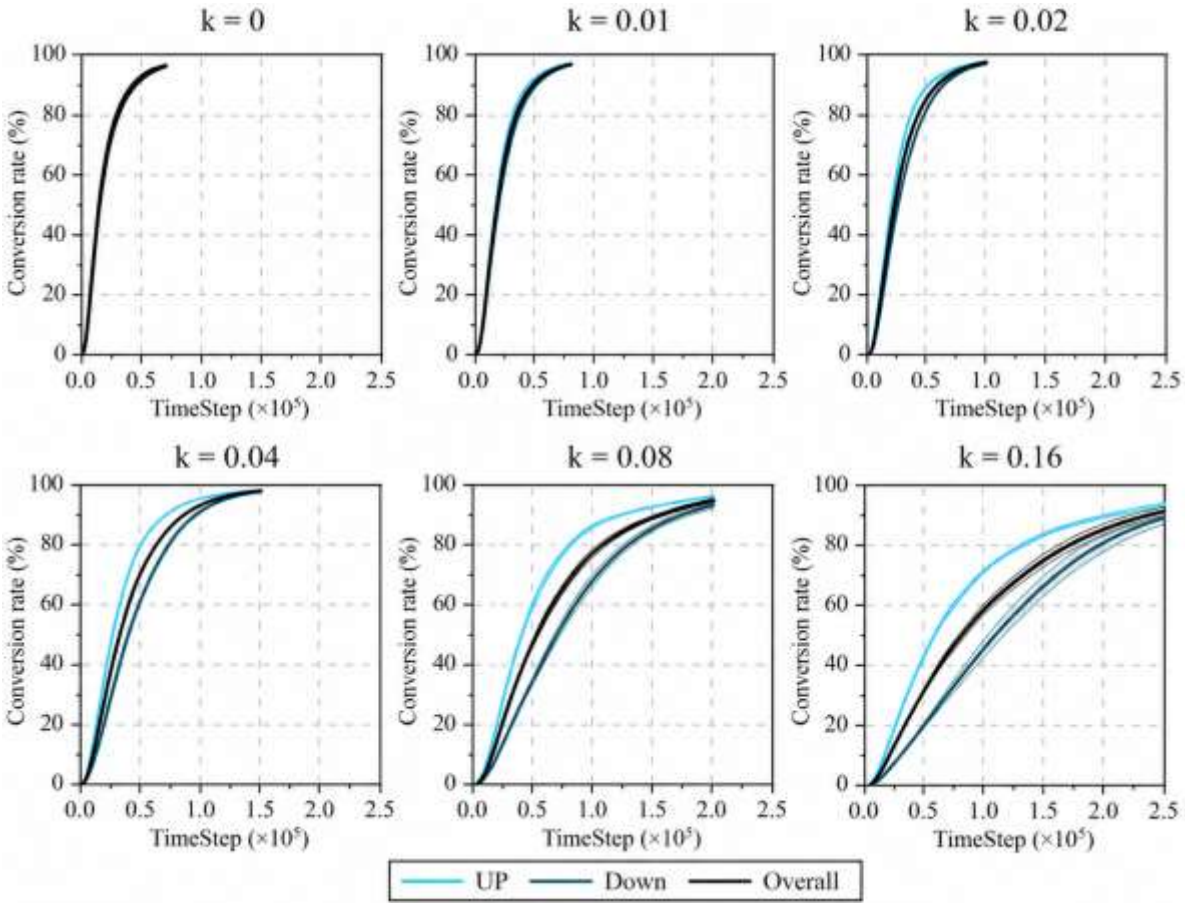

Figure 3. Conversion rate of monomers at different *k* values as a function of reaction time.

Figure 4 shows the evolution of initiator conversion as a function of reaction time, with the time corresponding to an overall monomer conversion of C_{on} = 90% explicitly marked. The apparent initiator conversion rate follows the same trend as monomer consumption, decreasing progressively with increasing *k*, which indicates that light attenuation markedly suppresses the photolysis process. When *k* = 0.16 and the overall monomer conversion of the system reaches 90%, the initiator conversion in the "UP" region is approximately 50%, whereas in the "Down" region it is only about 30%. This pronounced discrepancy further confirms that light attenuation governs the intrinsic mechanism underlying the gradient polymerization kinetics.

Figure 5 presents the evolution of the number of propagating radicals (R*) and terminated radicals (R_t) as a function of monomer conversion under different *k* conditions. The statistics were further resolved spatially for the "UP" and "Down" regions. The results indicate that, with increasing *k*, the overall population of propagating radicals decreases significantly. In the "UP" region, the peak number of propagating radicals drops progressively from approximately 100 at *k* = 0 to about 35 at *k* = 0.16.

The reduction is even more pronounced in the "Down" region, where the number of propagating radicals decreases to only around 10 at *k* = 0.16, highlighting the strong inhibitory effect of light attenuation on chain-growth activity. In contrast, terminated radicals exhibit a spatially differentiated response. In the "UP" region, for all *k* values, the number of terminated radicals at different monomer conversion stages shows minimal variation, and the corresponding evolution curves nearly overlap. However, in the "Down" region, the number of terminated radicals decreases continuously with increasing *k*.

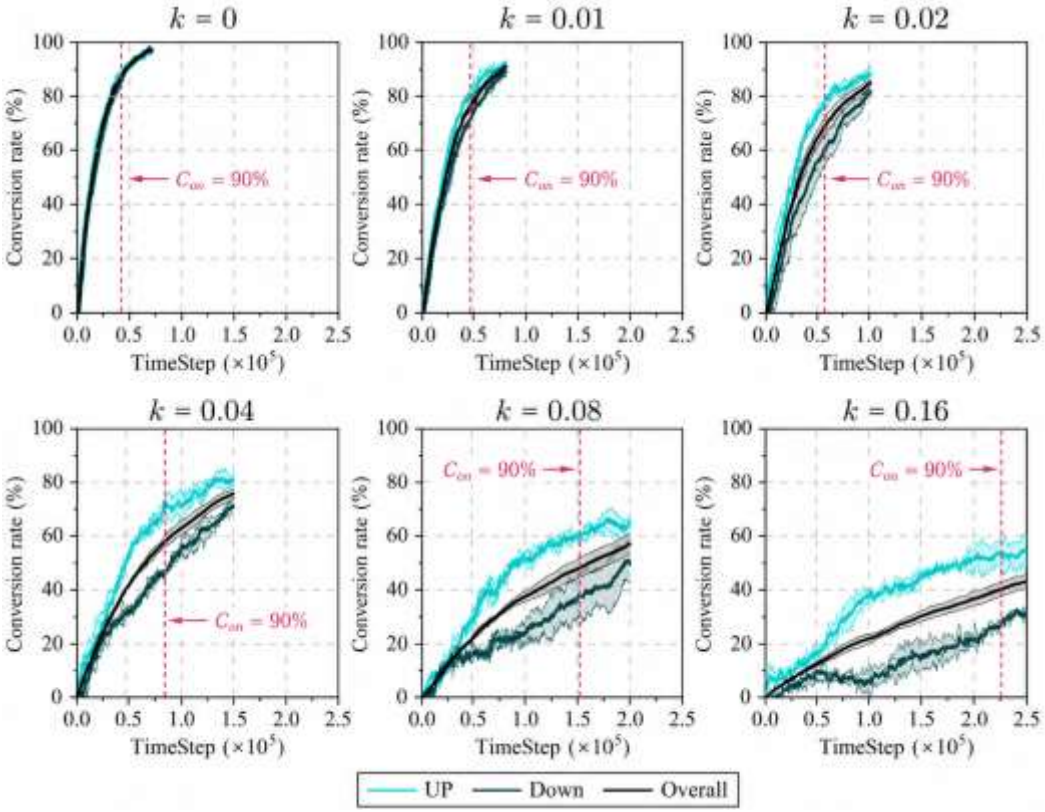

Figure 4. Conversion rate of initiators with different k values as a function of reaction time.

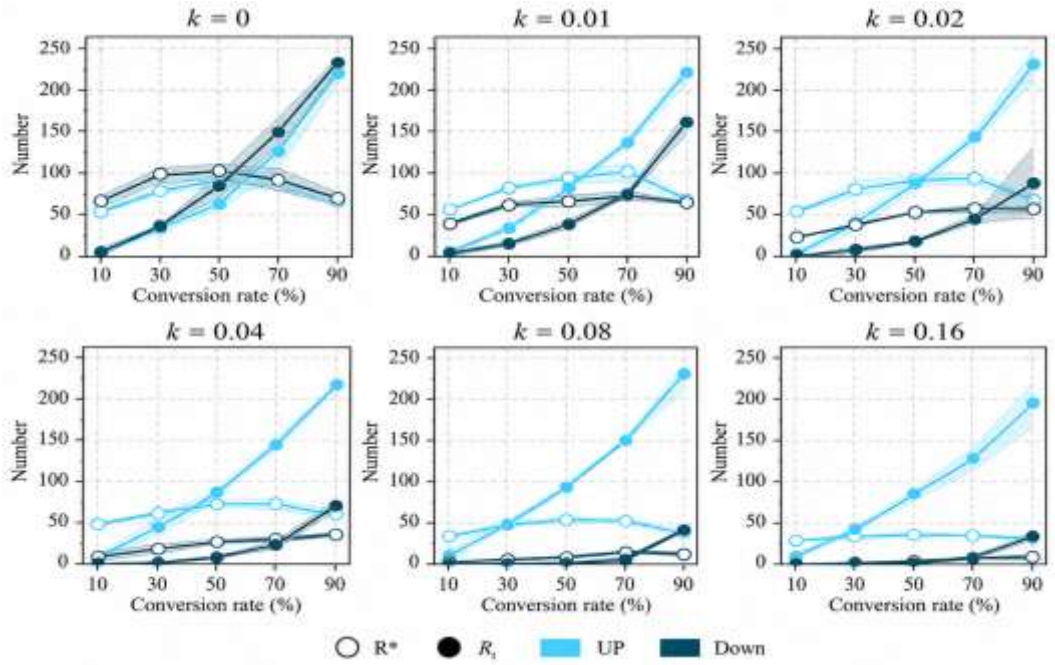

Figure 5. The number of propagating radicals R* and terminated radicals R_t with different k structures as a function of monomer conversion rate.

Structural Spatial Distribution Characteristics Induced by Gradient Aggregation

Figure 6 presents representative snapshots of the polymer chains formed at the early stage (C_{on} = 30%) and the late stage (C_{on} = 90%) under different k conditions. When k = 0, the light intensity is

spatially uniform, and radical generation occurs without positional selectivity. Molecular chains nucleate and grow randomly throughout the system. The resulting polymer clusters exhibit high spatial dispersion, and no evident regional gradient in structure is observed. As k increases, enhanced light attenuation induces a pronounced spatial bias in chain initiation toward the light-incident side. The spatial dispersion of polymer clusters decreases, interchain connectivity strengthens, and both structural compactness and network continuity progressively increase. Particularly under the strong attenuation condition ($k = 0.16$), even at the early reaction stage, the number of isolated molecular chains remains very low. Radicals preferentially form in the vicinity of pre-existing polymer structures and immediately participate in further growth or crosslinking reactions. At the late reaction stage, local morphological differences between the top and bottom regions become evident. The near-light ("UP") region exhibits densely packed and continuous chain structures, whereas the far-light ("Down") region retains a comparatively looser and less interconnected morphology, reflecting the persistent structural gradient induced by light attenuation.

Figure 7 presents the particle number distribution of the largest polymer cluster within ten equal segments along the z-axis (regions 1–10 correspond to consecutive statistical intervals from bottom to top). Overall, with increasing k, the slope of the particle distribution curve becomes progressively steeper, and the peak migrates towards the top region. This indicates that light attenuation significantly drives the enrichment of the largest polymer structure toward the light-incident side. At the early stage of polymerization (monomer conversion $\leq 30\%$), when $k \leq 0.02$, the particle distribution remains relatively flat, the largest cluster contains fewer particles, and no pronounced spatial feature is observed. However, once the monomer conversion reaches $\geq 50\%$, a clear divergence emerges between the $k = 0$ system and those with light attenuation. The former maintains a nearly uniform particle distribution along the z-axis, whereas the latter gradually develops a graded particle enrichment structure along the z-direction. When the monomer conversion reaches 90%, the trend of particle redistribution with increasing k becomes even more pronounced. Nevertheless, this effect approaches saturation around $k = 0.04$. Specifically, when $k \geq 0.04$, the particle number distributions of the largest cluster along the z-axis under different conditions largely overlap, indicating that further enhancement of light attenuation does not significantly alter the macroscopic spatial distribution of the dominant polymer network.

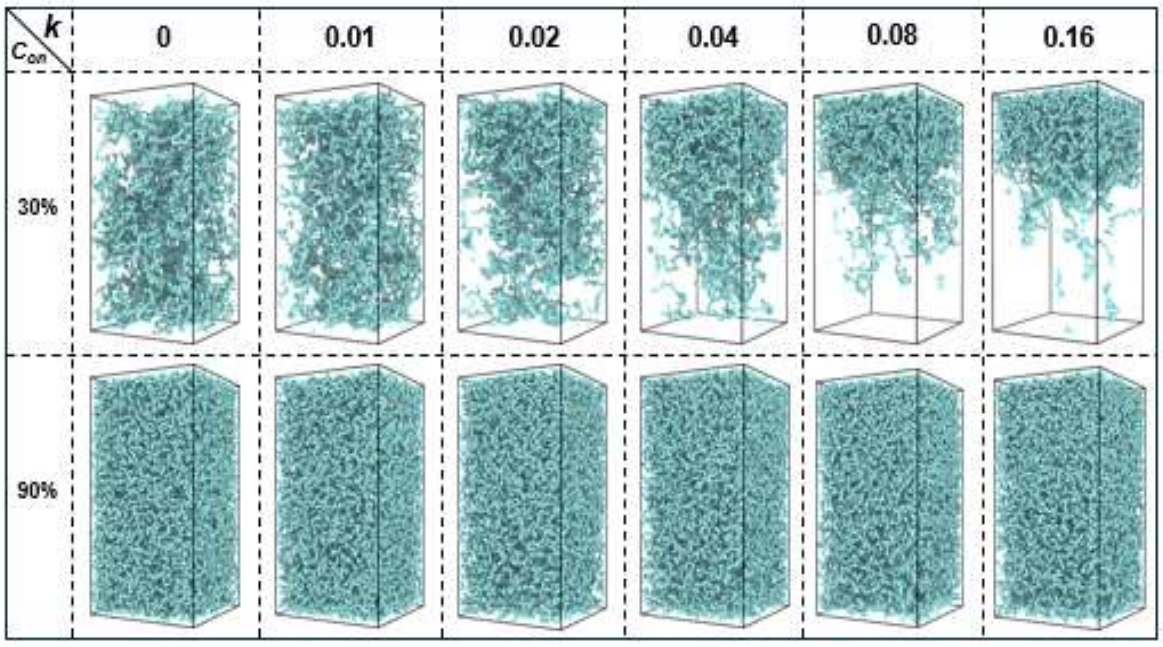

Figure 6. Snapshot of the polymerization process.

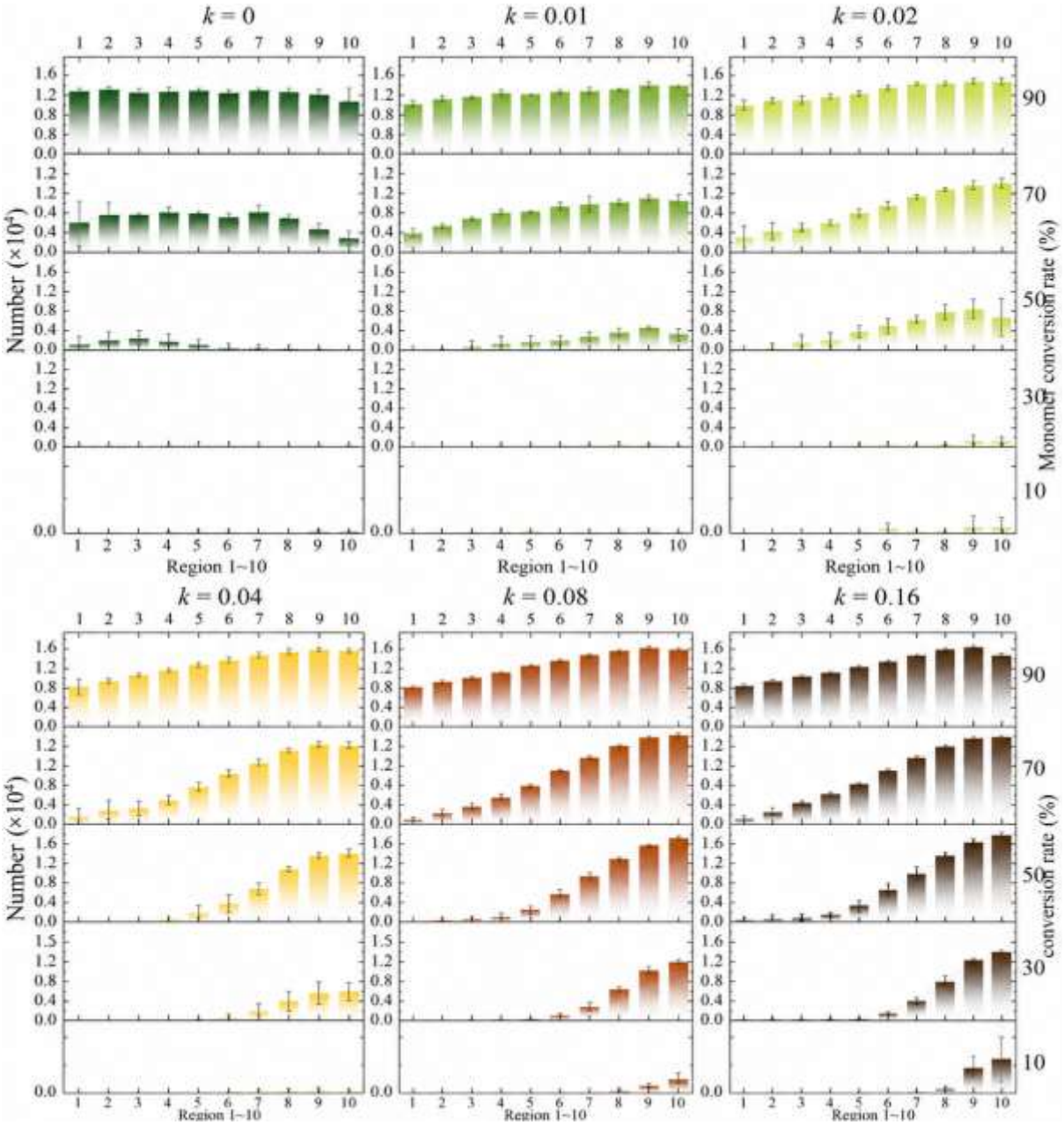

Figure 7. Distribution of structural particle numbers for different k values along the z-axis.

Spatial Gradient Characteristics of Cross-Linked Network Structures

Figure 8 presents the total number of particles and bonds in the stable network structures formed at a monomer conversion of 90% under different k conditions. The results show that the total number of particles incorporated into the stable structure increases overall with increasing k. This trend is consistent with the spatial distribution analysis of the largest cluster shown in Figure 7. When $k \geq 0.04$, the differences in structural particle numbers among the systems become negligible, indicating that the network size approaches a saturation state. A more detailed bond-type analysis reveals distinct behaviors.

The number of crosslinker characteristic bond ("C–X"), which reflects the total number of crosslinker molecules incorporated into the structure, reaches a maximum at $k = 0.04$ and subsequently decreases with further increases in k. In contrast, the number of "R–C" bonds—representing the actual participation of crosslinkers in effective reactions—exhibits a non-monotonic trend: under $k = 0.08$ and $k = 0.16$, the "R–C" bond number is higher than that at $k = 0.04$.

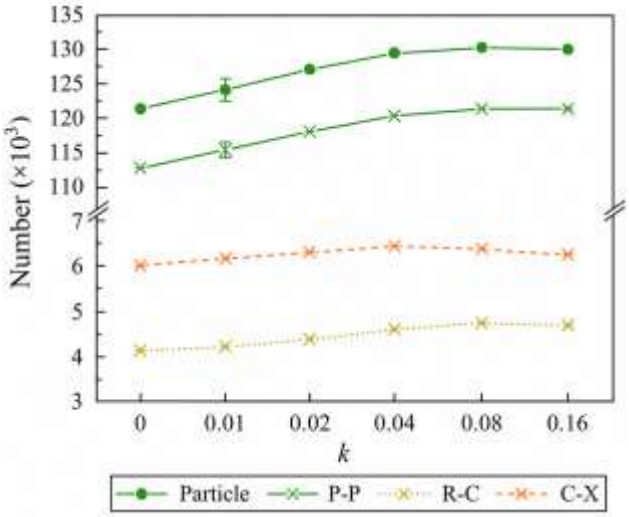

Figure 8. Statistics on particle and bond counts for structures at different *k* values.

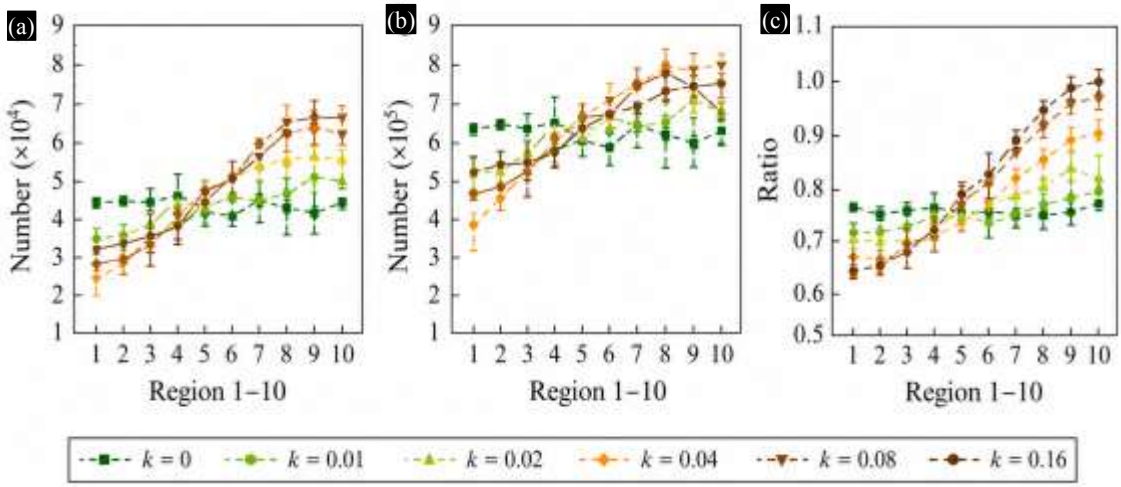

Figure 9. (a) Distribution of the number of cross-linking sites utilised; (b) Distribution of the total number of cross-linking sites; (c) Distribution of cross-linking site utilisation rates.

Figure 9 further quantifies the spatial distributions of used crosslinking sites, total crosslinking sites, and Crosslinking site utilisation rate along the *z*-axis. The results show that, with increasing *k*, the peaks of all three distributions progressively shift toward the top region of the simulation box, while the corresponding values in the bottom region continuously decrease. This trend reflects the pronounced spatial bias of crosslinking reactions under enhanced light attenuation. When $k \geq 0.04$, the number of used crosslinking sites in the top region becomes nearly identical across different *k* values. However, the total number of crosslinking sites begins to decrease once $k > 0.04$, directly supporting the inference that stronger light attenuation enables higher structural connectivity with fewer crosslinker molecules. As shown in Figure 9(c), the utilization efficiency of crosslinking sites in the high-light-intensity region increases markedly with increasing *k*. Although the bottom region exhibits relatively low crosslinker efficiency due to delayed local reactions, an additional effect emerges when $k > 0.04$. The prolonged diffusion time associated with polymerization retardation, combined with mass transport induced by network formation in the upper region, leads to significant crosslinker enrichment in the lower region. Consequently, the absolute numbers of both used crosslinking sites and crosslinker molecules in this region increase, despite the lower local reaction activity. These findings indicate that the light-field gradient not only governs the spatial location of crosslinking reactions but also reinforces the graded crosslinked network structure by redistributing crosslinker utilization efficiency throughout the system.

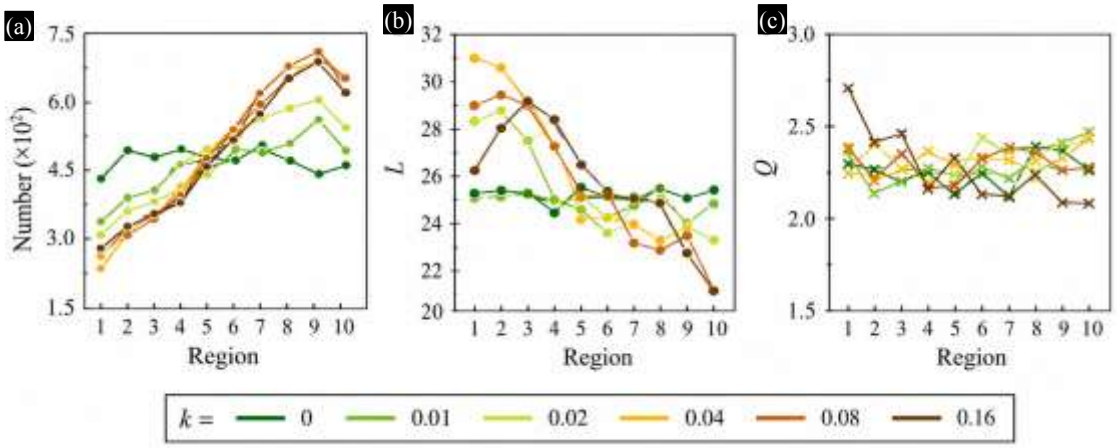

Figure 10. (a) Distribution of molecular chains between crosslinking sites; (b) Distribution of the average molecular chain length $\bar{L}$ between crosslinking sites; (c) Distribution of the dispersion index $Đ$ for molecular chain lengths between crosslinking sites.

Distribution Differences in Molecular Chain Size Between Cross-Linking Sites

Figure 10 presents the spatial distributions along the *z*-axis of the number of molecular chains between crosslinking sites, the average inter-node chain length ($\bar{L}$), and the dispersity index ($Đ$) at a monomer conversion of 90% under different *k* conditions, the green dashed line indicates the reference level for the $k = 0$ system. With increasing *k*, the number of molecular chains between crosslinking sites in the near-light region increases markedly and approaches a plateau when $k \geq 0.04$. In contrast, in the far-light bottom region, a slight upward trend is observed when $k > 0.04$. This behavior is strongly correlated with the spatial distribution of used crosslinking sites shown in Figure 9(a): the distributions in the top region nearly overlap for $k \geq 0.04$, while the bottom region exhibits an increase in used crosslinking sites, leading to a similar variation trend in the number of molecular chains between sites. The $\bar{L}$ exhibits a pronounced inverse spatial gradient with increasing *k*. In the top region, $\bar{L}$ decreases continuously and stabilizes once $k \geq 0.04$. In the bottom region, $\bar{L}$ also decreases when $k > 0.04$, which is associated with the increased number of used crosslinking sites. The spatial distribution of the dispersity index $Đ$, shown in Figure 10(c), reveals that, except for the strong attenuation case ($k = 0.16$), the overall differences in $Đ$ among various *k* conditions are not significant. When $k = 0.16$, a substantial disparity emerges between the near-light and far-light regions, indicating that the chain-length distribution between crosslinking sites is more concentrated in the near-light region, and the corresponding pore structure is more uniform than that in the bottom region. As observed in Figure 10(b), the spatial profiles of the $\bar{L}$ exhibit localized fluctuations, particularly within the lower zones (Regions 1–4) under intermediate attenuation coefficients. This statistical scatter is primarily attributed to the kinetic asynchrony of the system; the severe radical starvation and lower frequency of successful crosslinking events in the far-light region yield a smaller population of completed inter-node chain segments, thereby increasing the vulnerability of $\bar{L}$ to thermal noise and localized statistical variance across independent simulation trajectories.

DISCUSSION

Kinetic Asynchrony and Heterogeneous Radical Dynamics

The primary consequence of a non-uniform light field along the *z*-axis is the establishment of a sharp, position-dependent radical initiation rate. In a homogeneous system ($k = 0$), initiator decomposition occurs uniformly, giving rise to statistically symmetric polymer growth across all spatial regions. However, as the attenuation coefficient *k* increases, the primary locus of radical generation becomes tightly restricted to the near-light ("UP") region. This spatial restriction initiates a profound kinetic asynchrony within the material. This kinetic divergence is clearly demonstrated by the behavioral split of the propagating (R*) and terminated (R_t) radical populations under strong light attenuation ($k = 0.16$).

In the "UP" region, despite a lower peak value of active radicals caused by a lower average light intensity throughout the container, the duration of radical activity is extended due to a localized surplus of nearby unreacted monomers. Conversely, the "Down" region experiences extreme radical starvation. The depletion of monomers in this lower zone relies heavily on the physical transport and downward growth of living chain ends that originated in the "UP" region. Because local radical generation is suppressed in the far-light region, the frequency of radical-radical encounters drops drastically, resulting in a marked decline in disproportionation termination events (R_t). This creates a kinetic regime where the polymer network's growth is driven by a front-like propagation downward from the light-incident surface.

Topological Differentiation and Crosslinker Competition Mechanics

The spatial front of reaction rates translates into a permanent topological gradient in the finalized crosslinked network. The structural properties of the network sections are determined by a localized competition for chemical components. In the high-intensity near-light region, the rapid, simultaneous activation of multiple photoinitiators produces a dense cloud of early-stage growing radical clusters. These localized growing chains immediately consume the nearby crosslinkers. Because a large number of chain ends compete for a finite, uniformly distributed pool of crosslinkers within the same immediate volume, individual crosslinker beads are rapidly attacked from multiple sides. This competitive environment leads to a remarkable phenomenon: a sharp increase in the crosslinking site utilization efficiency (R-C bond formation) within the "UP" region, approaching 90% under strong attenuation (k = 0.16). However, because the crosslinkers are rapidly bound by a high density of growing chains, chain propagation is spatially hindered, forcing the near-light network to consist of highly dense, tightly crosslinked domains connected by very short average inter-node chains ($\bar{L}$). In contrast, the far-light ("Down") region undergoes a completely different structural pathway. Due to the delayed initiation front, crosslinkers in the lower region remain unreacted for an extended period, allowing for crosslinker mass transport toward the upper growing network. The living chains that eventually propagate into this lower zone encounter a low density of competing chain ends. Without intense spatial competition, these chains can grow much longer before hitting a crosslinking node, leading to large values of $\bar{L}$. Furthermore, because fewer radical ends are available to attack the remaining crosslinkers, the crosslinking site utilization efficiency in the bottom zone drops significantly. The resulting topology is an open, loosely crosslinked, large-pore network structure. This explicit dual-domain topology confirms that the sharpness of the light gradient directly dictates the breadth and uniformity (as measured by the dispersity index $Đ$) of the spatial network morphology.

Theoretical Guidance for Controllable Fabrication

These mesoscale findings offer important design principles for manufacturing functional gradient hydrogels or coatings with tailored network architectures and crosslinking distributions. The simulation reveals that the spatial structure of the largest cluster approaches a saturation threshold around k = 0.04. Beyond this value, further increasing the absorber concentration or molar absorption coefficient does not significantly change the overall mass distribution of the primary network, but it significantly changes the internal crosslinking efficiency and chain-length distributions ($\bar{L}$). These simulated results strongly corroborates experimental observations in the literature. For instance, it provides a molecular-level explanation for the spatial variations in monomer conversion that dictate the refractive-index gradients achieved by Tu et al [35]. via grayscale digital light processing (DLP). Similarly, this structural heterogeneity mirrors the depth-attenuated curing mechanisms utilized by Wen et al. [36], where severe light decay directly produces a stiff, highly crosslinked skin tier transitioning continuously into a compliant interior.

CONCLUSION

A coarse-grained model based on dissipative particle dynamics (DPD) was developed, in which light attenuation was explicitly coupled with free radical polymerization kinetics. The formation mechanism of gradient crosslinked networks induced by light attenuation and their corresponding spatial

topological evolution were systematically investigated. The results demonstrate that light attenuation governs the spatial distribution of radical generation, thereby serving as the fundamental driver of gradient structure formation. As the attenuation coefficient k increases, radical generation becomes progressively confined to the near-light region, resulting in asynchronous evolution of monomer consumption and chain propagation along the z-direction. This kinetic heterogeneity induces topological differentiation within the crosslinked network, giving rise under strong attenuation conditions to a characteristic structure featuring short-chain, highly crosslinked domains in the near-light region and long-chain, loosely crosslinked domains in the far-light region. Notably, while the total amount of incorporated crosslinker initially increases and subsequently decreases with rising k, the utilization efficiency of crosslinking sites is significantly enhanced in regions exposed to strong light attenuation. This finding uncovers a light-mediated spatial redistribution mechanism governing crosslinking efficiency.

GRAPHICAL SUMMARY

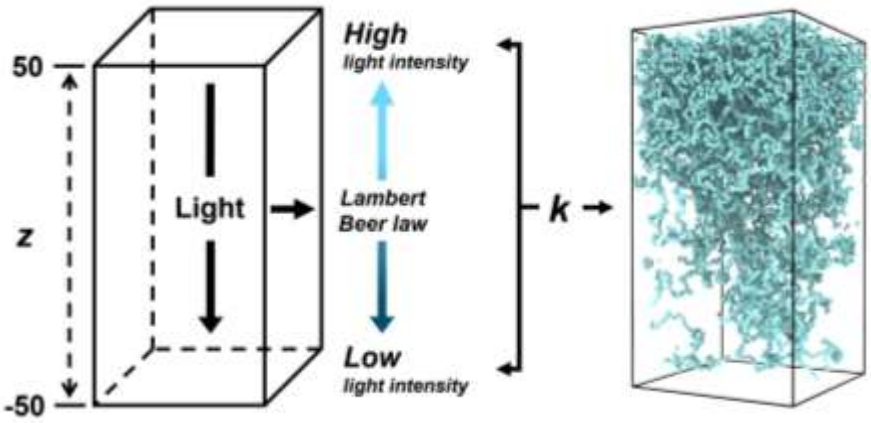

Acknowledgments

This work was supported by National Natural Science Foundation of China (No. 22463006); Qinzhou District Science and Technology Major Special Project in Tianshui City(2024-NCKJG-4929). Author Bingbing Pan and Zihua Liu contributed equally to this work and shoulder equal responsibility.

Data Availability Statement

The data generated during and analyzed during the current study are available from the corresponding author on reasonable request.

Declaim of Conflict of Interest

The authors declare no conflicts of interest regarding the publication of this paper.

REFERENCES

1. Gao R, Yu CC, Gao L, et al. A highly homogeneous polymer composed of tetrahedron-like monomers for high-isotropy expansion microscopy. Nat Nanotechnol. 2021;16(6):698–707. doi:10.1038/s41565-021-00875-7.
2. Yan X, Sun T, Song Y, et al. In situ thermal-responsive magnetic hydrogel for multidisciplinary therapy of hepatocellular carcinoma. Nano Lett. 2022;22(6):2251–2260. doi:10.1021/acs.nanolett.1c04413.
3. Wang L, Luo Y, Song Y, et al. Hydrogel-functionalized bandages with Janus wettability for efficient unidirectional drug delivery and wound care. ACS Nano. 2024;18(4):3468–3479. doi:10.1021/acsnano.3c10766.

4. Zhu H, Wang C, Yang Y, et al. High-strength mechanically gradient hydrogels via physical crosslinking for tendon-mimetic tissue repair. npj Flex Electron. 2025;9(1):53. doi:10.1038/s41528-025-00430-7.
5. Kosmidis PA, Chong SW, Shen Y, et al. Fabrication of gradient hydrogels using a thermophoretic approach in microfluidics. Biofabrication. 2024;16(2):025023. doi:10.1088/1758-5090/ad2b05.
6. O'Shea TC, Salem A, Schultz KM. A technique to create hydrogels with tethered concentration gradients of molecules in vitro. Soft Matter. 2026;22(3):678–691. doi:10.1039/D5SM01194A.
7. Ma Y, Wang Y, Chen D, et al. 3D bioprinting of a gradient stiffened gelatin-alginate hydrogel with adipose-derived stem cells for full-thickness skin regeneration. J Mater Chem B. 2023;11(13):2989–3000. doi:10.1039/D2TB02200A.
8. Zhang YC, Xue YQ, Ogawa T, et al. 3D printed alginate hydrogels with stiffness-gradient structure in a carbomer supporting bath by controlled Ca2+ diffusion. ACS Appl Eng Mater. 2023;1(2):802–812. doi:10.1021/acsaenm.2c00218.
9. Zhang YC, Xue YQ, Ogawa T, et al. Design and characterization of 3D printed pore gradient hydrogel scaffold for bone tissue engineering. Bioprinting. 2024;39:e00341. doi:10.1016/j.bprint.2024.e00341.
10. Wang W, Li H, Song P, et al. Photo-crosslinked integrated triphasic scaffolds with gradient composition and strength for osteochondral regeneration. J Mater Chem B. 2024;12(5):1271–1284. doi:10.1039/D3TB02031B.
11. Eckstein KN, Hergert JE, Uzcategui AC, et al. Controlled mechanical property gradients within a digital light processing printed hydrogel-composite osteochondral scaffold. Ann Biomed Eng. 2024;52(8):2162–2177. doi:10.1007/s10439-024-03516-x.
12. Liu JY, Yu JW, Chen HL, et al. Porous gradient hydrogel promotes skin regeneration by angiogenesis. J Colloid Interface Sci. 2024;671:312–324. doi:10.1016/j.jcis.2024.05.075.
13. Krishna DV, Sankar MR. Functionally graded Gelatine/PVA-based composite hydrogel for repairing the soft tissues of diarthrodial joints. Mater Today Commun. 2024;38:108070. doi:10.1016/j.mtcomm.2024.108070.
14. Gupta P, Waghmare S, Kar S, et al. Functionally gradient three-dimensional graphene foam-based polymeric scaffolds for multilayered tissue regeneration. RSC Adv. 2023;13(2):1245–1255. doi:10.1039/D2RA06018C.
15. Deng XB, Wei HX, Yang L, et al. Layered gradient-structured coating with sustained lubricating performance for the surface functionalization of implant materials. Chin J Polym Sci. 2025;43(6):1050–1058. doi:10.1007/s10118-025-3328-4.
16. Shirai Y, Sasaki A, Sato S, et al. Fabrication of an organic-inorganic hybrid hard coat with a gradient structure controlled by photoirradiation. ACS Appl Mater Interfaces. 2023;15(23):28563–28569. doi:10.1021/acsami.3c04399.
17. Yang XY, Jiang HJ, Zhong YT, et al. Hierarchically heterostructured ceramic cellular-polymer gradient coatings: Synergistic autonomous ice shedding and extreme-environment durability. J Colloid Interface Sci. 2025;695:137813. doi:10.1016/j.jcis.2025.137813.
18. Zhang WL, Yu F, Li XS, et al. Architectured gradient coupling of multiscale particles for high-performance superhydrophobic coatings. Surf Interfaces. 2026;82:108490. doi:10.1016/j.surfin.2026.108490.
19. Liu H, Chu H, Yuan H, et al. Bioinspired multifunctional self-sensing actuated gradient hydrogel for soft-hard robot remote interaction. Nano-Micro Lett. 2024;16(1):69. doi:10.1007/s40820-023-01287-z.
20. Zhu W, Wang J, Sun W, et al. Preparation of gradient hydrogel for pressure sensing by combining freezing and directional diffusion processes. Chem Eng J. 2023;451:138335. doi:10.1016/j.cej.2022.138335.
21. Zeng J, Jing X, Lin L, et al. Smart sensing hydrogel actuators conferred by MXene gradient arrangement. J Colloid Interface Sci. 2025;677:816-826. doi:10.1016/j.jcis.2024.08.117.
22. Song L, Wang Z, Chen S, et al. Phytic acid-induced gradient hydrogels for highly sensitive and broad range pressure sensing. Adv Mater. 2025;37(9):2417978. doi:10.1002/adma.202417978.

23. Ouyang K, Zhuang J, Chen C, et al. Gradient diffusion anisotropic carboxymethyl cellulose hydrogels for strain sensors. Biomacromolecules. 2021;22(12):5033–5041. doi:10.1021/acs.biomac.1c01003.
24. Huang K, Hung W, Su Y, et al. Zwitterionic gradient double-network hydrogel membranes with superior biofouling resistance for sustainable osmotic energy harvesting. Adv Funct Mater. 2023;33(19):2211316. doi:10.1002/adfm.202211316.
25. Yin J, Jia P, Ren Z, et al. Mechanically enhanced, environmentally stable, and bioinspired charge-gradient hydrogel membranes for efficient ion gradient power generation and linear self-powered sensing. Adv Mater. 2025;37(24):2417944. doi:10.1002/adma.202417944.
26. Wang Q, Huang J, Qi L, et al. A bioinspired gradient hydrogel electrolyte network with optimized interfacial chemistry toward robust aqueous zinc-ion batteries. ACS Nano. 2025;19(29):26770–26781. doi:10.1021/acsnano.5c06914.
27. Mao J, Iocozzia J, Huang J, et al. Graphene aerogels for efficient energy storage and conversion. Energy Environ Sci. 2018;11(4):772–799. doi:10.1039/C7EE03031B.
28. Li X, Sun F. An ultrastretchable gradient ionogel induced by a self-floating strategy for strain sensing. ACS Appl Mater Interfaces. 2023;15(31):37717–37727. doi:10.1021/acsami.3c06894.
29. Zhou Z, Xu Z, Zhang J, et al. An integrated capacitive pressure sensor based on gradient charge distribution with high sensitivity and fast response. ACS Appl Nano Mater. 2024;7(10):12043–12052. doi:10.1021/acsanm.4c01654.
30. Mezel M, Alsous MB, Abbas B, et al. Multimode gradient-index fiber coated with a blend of PEG and PVP as a humidity sensor. Results Opt. 2024;16:100697. doi:10.1016/j.rio.2024.100697.
31. Zinkovska N, Smilek J, Pekar M. Gradient hydrogels—the state of the art in preparation methods. Polymers. 2020;12(4):966. doi:10.3390/polym12040966.
32. Zhang Y, Wang H, Song Z, et al. Directed selective transport and enrichment of micropollutants by gradient hydrogels. J Hazard Mater. 2025;486:136929. doi:10.1016/j.jhazmat.2024.136929.
33. Jiang P, Zhang Y, Mu X, et al. Grayscale stereolithography of gradient hydrogel with site-selective shape deformation. Adv Mater Technol. 2022;7(7):2101288. doi:10.1002/admt.202101288.
34. Liu X, Liu S, Yang R, et al. Gradient chondroitin sulfate/poly(γ-glutamic acid) hydrogels inducing differentiation of stem cells for cartilage tissue engineering. Carbohydr Polym. 2021;270:118330. doi:10.1016/j.carbpol.2021.118330.
35. Tu J, Engelhardt JD, Barkow MH, et al. Additive manufacturing of polymeric gradient index optics via grayscale digital light processing vat photopolymerization technology. ACS Appl Opt Mater. 2025;3(6):1197–1207. doi:10.1021/acsaom.5c00143.
36. Wen T, Ma T, Qian J, et al. Phase-transition-induced dynamic surface wrinkle pattern on gradient photo-crosslinking liquid crystal elastomer. Nat Commun. 2024;15(1):10821. doi:10.1038/s41467-024-55180-3.
37. Shi R, Qian HJ, Lu ZY. Coarse-grained molecular dynamics simulation of polymers: Structures and dynamics. WIREs Comput Mol Sci. 2023;13(6):e1683. doi:10.1002/wcms.1683.
38. Bellussi FM, Ricci M, Fasano M, et al. Mesoscopic modeling of bio-compatible PLGA polymers with coarse-grained molecular dynamics simulations. J Phys Chem B. 2025;129(9):2598–2606. doi:10.1021/acs.jpcb.4c07518.
39. Li H, Gao K, Zhao H, et al. Dissipative particle dynamics study on the phase region of spatial gradient materials produced by photoinduced isomerization. Macromol Theory Simul. 2026;33(4):2400006. doi:10.1002/mats.202400006.
40. Deng W, Yu C, Guo H. Molecular dynamics simulation of self-assembly of one-component nanocrystals grafted with end-functionalized polymers. Soft Matter. 2026;22(8):1847–1862. doi:10.1039/D5SM01128K.
41. Groot RD, Warren PB. Dissipative particle dynamics: Bridging the gap between atomistic and mesoscopic simulation. J Chem Phys. 1997;107(11):4423–4435. doi:10.1063/1.474784.
42. Furuya T, Koga T. Molecular simulation of effects of network structure on fracture behavior of gels synthesized by radical polymerization. Macromolecules. 2025;58(7):3359–3368. doi:10.1021/acs.macromol.4c02875.

43. Zhang Z, Krajniak J, Dookhith AZ, et al. Topology and mechanical properties of polymer networks formed under free radical and atom transfer radical polymerizations. Macromolecules. 2025;58(6):3168–3187. doi:10.1021/acs.macromol.4c03138.
44. Hoogerbrugge PJ, Koelman JMVA. Simulating microscopic hydrodynamic phenomena with dissipative particle dynamics. Europhys Lett. 1992;19(3):155–160. doi:10.1209/0295-5075/19/3/001.
45. Müller M, Katsov K, Schick M. Biological and synthetic membranes: What can be learned from a coarse-grained description? Phys Rep. 2006;434(5–6):113–176. doi:10.1016/j.physrep.2006.08.003.
46. Li H, Zhao H, Gao K, et al. The conformational statistics of amphiphilic polymers with distinct topological structures at the interface between two phases. Polym Int. 2024;74: 152-162. doi: 10.1002/pi.6703.
47. Español P, Warren P. Statistical mechanics of dissipative particle dynamics. Europhys Lett. 1995;30(4):191–196. doi:10.1209/0295-5075/30/4/001.
48. Warren PB. Dissipative particle dynamics. Curr Opin Colloid Interface Sci. 1998;3(6):620–624. doi:10.1016/S1359-0294(98)80089-7.
49. Kröger M. Simple models for complex nonequilibrium fluids. Phys Rep. 2004;390(6):453–551. doi:10.1016/j.physrep.2003.10.014.
50. Groot RD, Madden TJ. Dynamic simulation of diblock copolymer microphase separation. J Chem Phys. 1998;108(20):8713–8724. doi:10.1063/1.476300.
51. Gavrilov AA, Chertovich AV. Simulation of the RAFT polymerization in 3D: Steric restrictions and incompatibility between species. Polym Chem. 2022;13(15):2143–2154. doi:10.1039/D1PY01624E.

